www.sciencemag.org/content/356/6335/295/suppl/DC1

Supplementary Material for

A parity-breaking electronic nematic phase transition in the spin-orbit coupled metal $Cd_2Re_2O_7$

J. W. Harter, Z. Y. Zhao, J.-Q. Yan, D. G. Mandrus, D. Hsieh*

*Corresponding author. Email: dhsieh@caltech.edu

Published 21 April 2017, *Science* **356**, 295 (2017)
DOI: 10.1126/science.aad1188

This PDF file includes:

Materials and Methods
Figs. S1 to S3
References

Materials and Methods

S1. Sample Growth and Characterization

Sample Growth

Single crystals of $Cd_2Re_2O_7$ were grown by vapor transport (*41*). X-ray diffraction measurements were performed on pulverized single crystals using a PANalytical X'Pert Pro powder x-ray diffractometer with Cu Kα radiation. No impurity peaks were observed. An elemental analysis was performed using a Hitachi TM-3000 scanning electron microscope equipped with a Bruker QUANTAX 70 energy dispersive x-ray system. The analysis confirmed an equal amount of Cd and Re within the resolution of the instrument. Magnetic susceptibility measurements were performed using a Quantum Design Magnetic Property Measurement System at temperatures ranging from 2 to 350 K. The results indicated high quality crystals without the presence of ReO_2 inclusions.

Stoichiometric Origin of SHG Heterogeneity

Wide-field SHG microscopy uncovered an inhomogeneous bulk response of the sample consisting of bright and dark regions. The boundaries between these regions are curved, tend to be near the edges of the sample, appear to be unaffected by structural domains, and have the same size scale as the single crystal itself. These facts strongly suggest chemical inhomogeneity during sample growth as a likely cause. To verify this hypothesis, we performed energy-dispersive x-ray spectroscopy (EDS) using an Oxford X-MaxN silicon drift detector attached to a Zeiss LEO 1550VP scanning electron microscope (SEM). This technique allows us to measure the spatially-resolved chemical composition of the sample near its surface. We collected EDS spectra at eight points—four inside a dark region and four inside a bright region—near a well-defined feature on the (111) sample surface, as shown in Fig. S1.

A typical EDS spectrum is shown in Fig. S1C. Peaks from O, Cd, and Re atoms can be identified, and fitting the spectrum allows us to infer the atomic percentages of the atoms at each sample location. Our results are summarized in the following table:

Location	Region	O atomic %	Cd atomic %	Re atomic %	Cd/Re ratio
1	Dark	61.85	19.17	18.98	1.0100
2	Bright	64.31	18.14	17.55	1.0336
3	Bright	62.39	19.08	18.53	1.0297
4	Dark	62.75	18.82	18.43	1.0212
5	Bright	62.52	19.08	18.40	1.0370
6	Dark	62.09	19.06	18.85	1.0111
7	Bright	60.86	19.73	19.41	1.0165
8	Dark	61.16	19.56	19.28	1.0145

Variability of oxygen stoichiometry is a known issue in the growth of $Cd_2Re_2O_7$ (*41*) and is a prime candidate for the origin of the heterogeneity, but the oxygen atomic percentage does not appear to correlate with the bright and dark regions within the resolution of our experiment. We do detect, however, a difference in the average Cd/Re atomic ratio: 1.029 ± 0.009 in the bright region and 1.014 ± 0.005 in the dark region. A Student's *t*-test of the data shows that the difference is statistically significant ($p = 0.027$). The measured deviations of the Cd/Re ratio from 1 are within the *absolute* accuracy of the EDS instrument, so we cannot determine which of the two regions is more stoichiometric.

In oxide pyrochlores with chemical formula $A_2B_2O_7$, the A and B cations can intermix under certain conditions and may even form a stable disordered phase (*42*). Indeed, in so-called "stuffed spin-ice" pyrochlores, the A/B atomic ratio can exceed 1.9 (*43*). Given our various observations as a whole, the most likely scenario is that inhomogeneous growth conditions cause Re atoms, with a much smaller ionic radius, to occupy some of the Cd sites in the darker regions of the sample. This will cause the nanoscale crystallinity to be slightly worse there (and may result in some localized metallic doping). It is then natural to expect the order parameter to be weaker in the more disordered regions of the sample, as we observe. For this reason, our study focuses on bright regions, where the bulk order parameters are larger with respect to the surface term.

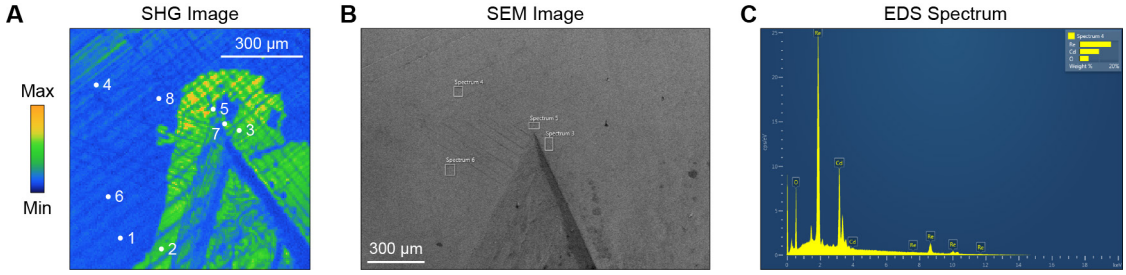

Fig. S1. Spatial mapping of sample stoichiometry. (**A**) SHG image of the sample at 150 K near a well-defined feature on the surface. Eight sample points in bright and dark regions measured with EDS are indicated. (**B**) SEM image showing four of the rectangular regions used for EDS measurements. (**C**) Typical EDS spectrum, with x-ray peaks identified for O, Cd, and Re atoms.

S2. Wide-Field SHG Microscopy

Wide-field SHG imaging was performed using ultrashort 100 fs optical pulses with a center wavelength of 800 nm produced at a 100 kHz repetition rate by a regeneratively-amplified Ti:sapphire laser system (Coherent Vitara-S and RegA 9050). The beam illuminated the entire (111) sample facet at an oblique 20° angle of incidence and with a fluence below 30 μJ cm^{-2}. The reflected second-harmonic light was selected with a 400 nm narrow bandpass filter and linear polarizer, collected by an objective lens, and focused onto an EM-CCD camera (Andor iXon Ultra 897). Each pixel in the image captured a 6 × 6 μm^2 area on the sample surface. Upon temperature cycling, we did not observe any movement of tetragonal domains, suggesting that they are pinned by static strain fields and other crystallographic defects.

S3. RA-SHG Measurements

RA-SHG measurements were performed with the same 800 nm light source as that used for the microscopy measurements. Both the sample and detector remained fixed. Rotation of the scattering plane was achieved by mechanically spinning transmissive optical elements about the central beam axis. A detailed description of the novel RA-SHG apparatus used can be found in Ref. *34*. The laser was obliquely incident on the sample with a fixed 10° angle between the beam and the sample surface normal. The fluence of the beam was maintained at 600 μJ cm^{-2}, with no noticeable degradation of the sample with time. The laser spot size on the sample was 30 μm full-width at half-maximum. Reflected second-harmonic light at 400 nm was selected with a narrow bandpass filter and measured with a two-dimensional EM-CCD (Andor iXon Ultra 897). Each complete RA pattern was acquired with a 30 s exposure time. Samples were measured in an optical cryostat with a vacuum pressure below 10^{-6} Torr. We point out that an 800 nm wavelength ($\hbar\omega = 1.5$ eV) is resonant with interband transitions between occupied O 2*p* and unoccupied Re 5*d* states in $Cd_2Re_2O_7$ (*44–46*), significantly enhancing the SHG response of the crystal at this wavelength. We did not observe substantial steady-state heating of the sample based on the close agreement between T_c measured using SHG and T_c previously reported in the literature (*26*). This is consistent with a calculation of the heating amount (~ 2 K) using a thermal conductivity of 3 W m^{-1} K^{-1} (*47*).

S4. Identification of All Six Domain Types

A cubic-to-tetragonal distortion will in general result in three types of domains, with each aligned along one of the three equivalent cubic lattice directions in the crystal. In addition, a parity-breaking distortion can occur in two separate ways related by inversion symmetry. Aided by SHG imaging, we are indeed able to find all six possible types of structural domains (three tetragonal × two parity) on the (111) sample surface. Performing RA-SHG measurements at each of the six domains yields distinct RA patterns, allowing us to fully distinguish them, as shown in Fig. S2.

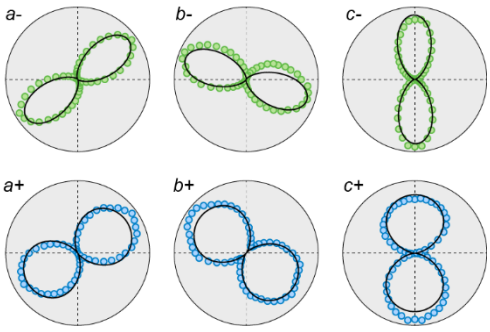

Fig. S2. Identification of domains via RA-SHG. Normalized S_{in}–P_{out} RA-SHG patterns measured at 150 K at various locations on the sample surface showing all six possible structural domains. The three types of tetragonal domains (*a*, *b*, *c*) are distinguished by the directions of the RA lobes, which differ by 120°. The two types of parity domains (+, –) are distinguished by the shapes of the RA lobes, which differ because of interference between bulk and surface SHG.

S5. RA-SHG Data for All Four Polarization Geometries

To minimize systematic errors, we use all four linear polarization geometries when fitting the nonlinear susceptibility to the data. At each temperature, all four RA patterns (P_{in}–P_{out}, P_{in}–S_{out}, S_{in}–P_{out}, and S_{in}–S_{out}) are measured and fit simultaneously with the *same* set of free parameters. Fig. S3 displays RA patterns and resulting fits for a representative selection of temperatures taken at (+) and (–) domains in dark regions of the sample, as well as a (–) domain in a bright region of the sample. Notably, there is no detectible bulk response for S_{in}–S_{out}. We use this fact to constrain some of the bulk susceptibility components, as discussed in S6 below. Parity domains can be clearly distinguished from each other by the anisotropy resulting from interference with the surface SHG component. Because the bulk response is much stronger relative to the surface in the bright regions, our sensitivity to bulk symmetry breaking near T_c is increased there.

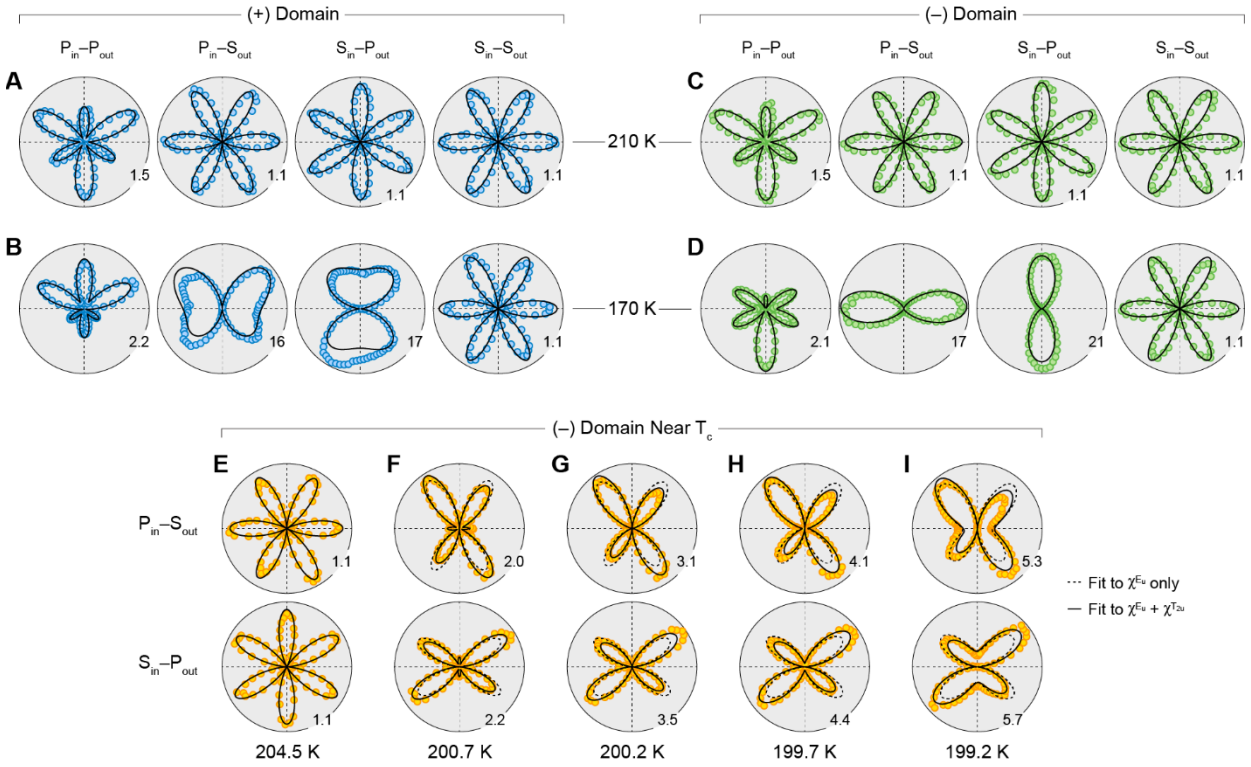

Fig. S3. RA-SHG domain contrast. (**A**)-(**D**) RA-SHG data with all four polarization geometries for a (+) domain (A, B) and a (–) domain (C, D) taken above T_c at 210 K (A and C) and below T_c at 170 K (B and D). At high temperatures, only the surface SHG contributes and the two domains are identical. Below T_c, interference between the static surface and growing bulk SHG contributions generates RA contrast between the parity domains. (**E**)-(**I**) P_{in}–S_{out} and S_{in}–P_{out} RA-SHG data taken at 204.5 K (E), 200.7 K (F), 200.2 K (G), 199.7 K (H), and 199.2 K (I). The loss of horizontal reflection symmetry in the RA curves is clearly detected below T_c but is not captured by fitting the data to a $\bar{4}2m$ bulk point group (dashed curves). A $\bar{4}$ bulk point group, however, fits the data well (solid curves).

S6. Surface and Bulk Susceptibility Tensors

In our RA-SHG measurements, we observe a static, temperature-independent SHG component from inversion symmetry breaking at the sample surface. To isolate this component from the bulk response, we split the second-order optical susceptibility tensor that we measure into surface and bulk parts. Optical susceptibilities are complex. Our experiments, however, are only sensitive to relative phase differences between the susceptibility components, so we define the surface part to be strictly real but allow a complex phase for the bulk: $\chi_{ijk}^{measured} = \chi_{ijk}^{S} + \chi_{ijk}^{B}$.

In the cubic phase, the (111) surface of $Cd_2Re_2O_7$ contains three mirror planes and a three-fold rotation axis and is represented by point group $3m$. This symmetry group, together with SHG permutation symmetry, restricts the possible nonzero tensor elements of χ_{ijk}^{S} to $\chi_{xxz} = \chi_{xzx} = \chi_{yyz} = \chi_{yzy}$, $\chi_{zxx} = \chi_{zyy}$, $\chi_{yxx} = \chi_{xxy} = \chi_{xyx} = -\chi_{yyy}$, and χ_{zzz}, where coordinate axes are chosen so that one of the mirror planes is perpendicular to the *x*-axis and the surface normal is parallel to the *z*-axis (*30*). At high temperatures, where only χ_{ijk}^{S} is nonzero, we find best agreement with our data when $\chi_{xxz} = -0.9$, $\chi_{zxx} = 0$, and $\chi_{zzz} = 200$, in units where $\chi_{yyy} = 1$. We fix these values during our low-temperature fits and do not let them vary. In the *y*-axis labels of Fig. 4, "$|\chi^{S}|$" is shorthand for the value of the χ_{yyy} surface tensor element.

Our experiments show that χ_{ijk}^{B} cannot be faithfully represented by a point group of higher symmetry than $\bar{4}$, whose nonzero tensor elements are $\chi_{xxz} = \chi_{xzx} = -\chi_{yyz} = -\chi_{yzy}$, $\chi_{xyz} = \chi_{xzy} = \chi_{yxz} = \chi_{yzx}$, $\chi_{zxx} = -\chi_{zyy}$, and $\chi_{zxy} = \chi_{zyx}$ (*30*). Here, the coordinate axes *x*, *y*, and *z* are chosen to be aligned with the cubic crystallographic directions *a*, *b*, and *c*, respectively. As discussed in the main text, it is physically more appropriate to split this general bulk tensor into two parts, labeled $\chi_{ijk}^{E_u}$ and $\chi_{ijk}^{T_{2u}}$, that transform like point groups $\bar{4}2m$ (the isotropy group induced by E_u order) and $\bar{4}m2$ (the isotropy group induced by T_{2u} order), respectively. Strictly speaking, these point groups are synonymous, differing by a trivial 45° rotation about the $\bar{4}$ axis. Within a *space* group, however, the cubic crystallographic axes define fixed directions in space and the two become inequivalent. This decomposition of the $\bar{4}$ tensor can be performed without loss of generality and unambiguously because $\bar{4}2m$ tensors contain only $\chi_{xyz} = \chi_{xzy} = \chi_{yxz} = \chi_{yzx}$ and $\chi_{zxy} = \chi_{zyx}$ and $\bar{4}$m2 tensors contain only $\chi_{xxz} = \chi_{xzx} = -\chi_{yyz} = -\chi_{yzy}$ and $\chi_{zxx} = -\chi_{zyy}$. In particular, no tensor elements are shared between the two point groups.

We observe an additional symmetry in the χ_{ijk}^{B} tensor: $\chi_{zxy} = -2\chi_{xyz}$ and $\chi_{zxx} = -2\chi_{xxz}$. Experimentally, this symmetry is manifest in the complete absence of bulk SHG for the S_{in}–S_{out} polarization geometry (see S5 above). For $\chi_{ijk}^{E_u}$, this constraint is directly related to the fact that a general $\bar{4}2m$ tensor transforms like the direct sum $E_u \oplus A_{2u}$. By setting $\chi_{zxy} = -2\chi_{xyz}$, the A_{2u} part is projected out of the susceptibility tensor. For $\chi_{ijk}^{T_{2u}}$, the constraint $\chi_{zxx} = -2\chi_{xxz}$ is not imposed by T_{2u} macroscopic symmetry considerations alone, but may follow from symmetries in the microscopic Hamiltonian. A further discussion of these additional symmetries can be found in S7 below.

In the end, only two independent complex parameters are allowed to vary with temperature in the susceptibility model that we employ: χ_{xxz} and χ_{xyz}. In the *y*-axis labels of Fig. 4, "$|\chi^{E_u}|$" is shorthand for the magnitude of the χ_{xyz} bulk tensor element and "$|\chi^{T_{2u}}|$" is shorthand for the magnitude of the χ_{xxz} bulk tensor element.

S7. Linear Proportionality of Bulk Susceptibility and Odd-Parity Order Parameters

For a parity-breaking phase transition, we expect the bulk second-order optical susceptibility tensor to be linearly proportional to the order parameter for temperatures sufficiently close to T_c. The susceptibility, like the order parameter, is zero in the high-temperature centrosymmetric phase and nonzero in the low-temperature noncentrosymmetric phase. Furthermore, if the order parameter reverses sign, for example in different parity domains related by spatial inversion, so does the susceptibility. We have observed this sign reversal in our measurements and it allows us to distinguish (+) and (–) domains, as shown in S5 above. This means that a generic series expansion of the susceptibility in the order parameter will include only odd powers, with a linear term being the first allowed.

A more rigorous proof that the nonlinear optical susceptibility is linearly proportional to the odd-parity order parameters may be obtained by expanding the Landau free energy up to lowest order in powers of components of the electric polarization **P** (a polar vector transforming like T_{1u}) and the odd-parity order parameters Ψ_u (representing T_{2u} order) and Φ (representing E_u order) (*48*):

$$F(\mathbf{P}) = F_0 + \frac{a}{2}P_iP_i - E_iP_i - b\Psi_u F_1(\mathbf{P}) - c\Phi F_2(\mathbf{P}) + \cdots,$$
$$F_1(\mathbf{P}) = \left(P_x^2 - P_y^2\right)P_z\left[1 - dP_z^2/\left(P_x^2 + P_y^2 + P_z^2\right)\right],$$
$$F_2(\mathbf{P}) = P_xP_yP_z\left[1 - 3P_z^2/\left(P_x^2 + P_y^2 + P_z^2\right)\right],$$

where summation over repeated indices is implied, **E** is the externally applied optical electric field, $a > 0$ because the system is not ferroelectric, *b* and *c* are constants coupling the electric polarization to the T_{2u} and E_u order parameters, respectively, and *d* is a dimensionless constant determined by the microscopic Hamiltonian of the system. Minimizing the free energy with respect to variation of the components of the electric polarization gives

$$P_i = \frac{1}{a}E_i + \left(\frac{b\Psi_u}{a}\right)\frac{\partial F_1}{\partial P_i} + \left(\frac{c\Phi}{a}\right)\frac{\partial F_2}{\partial P_i}.$$

By noting that $P_i = \chi_{ij}E_j + \chi_{ijk}E_jE_k + \cdots$, we may write

$$\chi_{ijk} = \frac{1}{2}\frac{\partial^2 P_i}{\partial E_j \partial E_k}\bigg|_{E=0} = \frac{1}{2a^2}\lim_{P_i\to 0}\lim_{P_j\to 0}\lim_{P_k\to 0}\frac{\partial^2 P_i}{\partial P_j \partial P_k}.$$

This formula gives $\chi_{xyz} = \chi_{xzy} = \chi_{yxz} = \chi_{yzx} = -\chi_{zxy}/2 = -\chi_{zyx}/2 = c\Phi/2a^3$, explicitly showing the linear proportionality of χ^{E_u} and Φ and confirming the additional symmetry constraint $\chi_{zxy} = -2\chi_{xyz}$ discussed in S6 above. We also obtain $\chi_{xxz} = \chi_{xzx} = -\chi_{yyz} = -\chi_{yzy} = b\Psi_u/a^3$ and $\chi_{zxx} = -\chi_{zyy} = (1-d)b\Psi_u/a^3$, showing the proportionality of $\chi^{T_{2u}}$ and Ψ_u.

Interestingly, the empirical relation $\chi_{zxx} = -2\chi_{xxz}$ that we observe in our measurements is achieved if $d = 3$, which is likely the result of a microscopic symmetry in the Hamiltonian of the system and offers a strong constraint on possible theories of the multipolar nematic phase in $Cd_2Re_2O_7$.

S8. Landau Theory Symmetry Analysis

Within Landau's theory of second-order phase transitions, an order parameter Φ that grows linearly with temperature in the low-symmetry phase, $\Phi \propto (1 - T/T_c)$ for $T < T_c$, must be secondary, induced by a coupling to a primary order parameter Ψ with mean field temperature dependence $\Psi \propto \sqrt{1 - T/T_c}$ (*49*). The so-called "faintness index" $n \geq 2$ encodes the exponent of the primary order parameter that couples to the secondary order parameter in the Landau free energy, producing an invariant term of the form $\Psi^n\Phi$ (*50*). Ferroic transitions that occur under these conditions are labeled "improper" (*49–51*). In particular, for a secondary order parameter with linear temperature dependence, $n = 2$.

A parity-breaking secondary order parameter with $n = 2$ implies the existence of exactly two coupled primary order parameters, one that breaks inversion symmetry and one that preserves it. This is because a term like $\Psi^2\Phi$ is not invariant under the parity operation if Φ breaks inversion symmetry. In analogy with Mulliken notation, let us call the parity-even order parameter Ψ_g and the parity-odd order parameter Ψ_u. Then a coupling term like $\Psi_g\Psi_u\Phi$ is invariant with respect to inversion symmetry and is allowed in the Landau free energy

$$F(T) = F_0 - \frac{a}{2}\left(1 - \frac{T}{T_c}\right)\left(\Psi_g^2 + \Psi_u^2\right) + \frac{b}{2}\Phi^2 - g\Psi_g\Psi_u\Phi + \frac{c}{4}\left(\Psi_g^4 + \Psi_u^4\right) + \cdots,$$

where a, b, and c are positive constants to guarantee a stable solution and g controls the strength of the coupling between the primary and secondary order parameters. For convenience, we have taken the expansion coefficients of Ψ_g and Ψ_u to be identical ($a_g = a_u$) and have ignored higher-order terms in the expansion; such simplifications are irrelevant to the arguments that follow. It should be noted, however, that the identical temperature dependence of the leading order coefficients for the primary order parameters—positive above T_c and negative below T_c—ensures that Ψ_g and Ψ_u become nonzero at the same temperature. Although not strictly guaranteed by theoretical arguments alone, such a condition is realized in practice if the coupled primary orders have the same physical origin. For example, the improper ferroelectric transitions observed in $PbTiO_3/SrTiO_3$ superlattices and $(Ca,Sr)_3Ti_2O_7$ are driven by the simultaneous freezing of two phonon modes of different one-dimensional irreducible representations, one preserving inversion symmetry and the other breaking it (*52, 53*).

Minimization of the free energy with respect to variation of the order parameters gives

$$\Psi_g(T) = \Psi_u(T) = \sqrt{\frac{ab}{bc - g^2}}\sqrt{1 - \frac{T}{T_c}}, \quad \Phi(T) = \left(\frac{ag}{bc - g^2}\right)\left(1 - \frac{T}{T_c}\right).$$

By construction, we obtain a linear temperature dependence for the secondary order parameter Φ. Higher-order terms in the free energy expansion or differing coefficients for Ψ_g and Ψ_u will, in general, change the constant factors in the above expressions but will not change the temperature dependence near T_c. This analysis shows that in $Cd_2Re_2O_7$, the E_u structural distortion occurring at the 200 K phase transition (here represented by Φ) must be driven by a pair of primary order parameters Ψ_g and Ψ_u.

To proceed further, we impose four rules constraining the irreducible representations of the primary order parameters Ψ_g and Ψ_u.

- **Rule #1:** The Landau condition must hold, which states that for a second-order phase transition, no third-degree term can appear in the free energy expansion. This eliminates the A_{1g}, E_g, and T_{2g} irreducible representations for Ψ_g (*54*).
- **Rule #2:** Ψ_u cannot transform like E_u. Otherwise, the term $\Psi_u\Phi$ would occur in the free energy and the transition would not be improper (Φ would have a square-root temperature dependence).
- **Rule #3:** In order for $\Psi_g\Psi_u\Phi$ to be an allowed invariant in the free energy, the symmetric direct product of the irreducible representations for Ψ_g and Ψ_u must contain E_u.

These first three rules immediately imply that Ψ_g must transform like T_{1g}, and leave only two possibilities for the irreducible representation of Ψ_u: T_{1u} or T_{2u}. We now invoke the so-called "maximal isotropy group condition" (*51*), which states that because Ψ_g and Ψ_u transform like multidimensional irreducible representations, their directions in order parameter space must correspond to a maximal isotropy subgroup. Thus, we restrict our attention to the tetragonal isotropy subgroups that result from order parameter directions aligned with one of the cubic crystallographic axes. The E_u structural order parameter in $Cd_2Re_2O_7$ is two-dimensional, but only the $E_u^{(2)}$ partner is observed by structure-sensitive probes. This fact leads to a final rule that allows us to resolve the ambiguity in the symmetry of the Ψ_u order parameter.

- **Rule #4:** In the free energy expansion, $\Psi_g\Psi_u$ cannot couple to the structural partner $E_u^{(1)}$. Otherwise, it would be finite below T_c and detected by experiment.

Only one pair of order parameter symmetries is consistent with this final rule: Ψ_g transforms according to T_{1g} in the $\langle 001 \rangle$ direction [isotropy subgroup $I4_1/a$ (*48*)] and Ψ_u transforms according to T_{2u} in the $\langle 001 \rangle$ direction [isotropy subgroup $I\bar{4}2d$ (*48*)]. The maximal common subgroup of the order parameter isotropy groups is $I\bar{4}$, which is the true space group of $Cd_2Re_2O_7$ in the low temperature phase.

We emphasize that this analysis, which is based solely on the observed linear temperature dependence of the E_u order parameter, necessitates the existence of a T_{2u} primary order parameter and therefore serves as a strong self-consistency check of our observations. This symmetry-based evidence of T_{2u} order also predicts the existence of a coupled T_{1g} primary order. The apparent coupling between the T_{2u} and T_{1g} primary orders suggests that they have a similar physical origin,

and we now discuss a possible mechanism for T_{1g} electronic order in $Cd_2Re_2O_7$ (T_{1g} transforms like a rotation, such as an angular momentum). Re^{5+} ions have a $5d^2$ valence configuration. Density functional theory calculations show that the octahedral crystal field strongly splits the $5d$ orbitals, pushing the unoccupied e_g states ~ 5 eV higher in energy than the occupied t_{2g} states (*44–46*). If we consider a single Re^{5+} ion in isolation, the spatial part of the two-valence-electron wave function will transform according to the direct product $t_{2g} \otimes t_{2g} = A_{1g} + E_g + [T_{1g}] + T_{2g}$, where the brackets denote the antisymmetric combination. According to Hund's first rule, electron interactions will favor the spin triplet state with term symbol ${}^3T_{1g}$ (*55*). Although the preceding argument applies only to isolated ions, we anticipate that within $Cd_2Re_2O_7$ interactions among electrons in the Re t_{2g} levels may favor a correlated triplet state with T_{1g} symmetry. A nuclear quadrupole resonance experiment indeed detected a moderate ferromagnetic enhancement, but no static magnetic order was observed (*37*), calling a simple spin triplet state into question. More theoretical work is necessary to identify a suitable physical mechanism for T_{1g} electronic order.

References and Notes

1. E. Fradkin, S. A. Kivelson, M. J. Lawler, J. P. Eisenstein, A. P. Mackenzie, Nematic Fermi fluids in condensed matter physics. *Annu. Rev. Condens. Matter Phys.* **1**, 153–178 (2010). doi:10.1146/annurev-conmatphys-070909-103925

2. M. P. Lilly, K. B. Cooper, J. P. Eisenstein, L. N. Pfeiffer, K. W. West, Evidence for an anisotropic state of two-dimensional electrons in high Landau levels. *Phys. Rev. Lett.* **82**, 394–397 (1999). doi:10.1103/PhysRevLett.82.394

3. R. R. Du, D. C. Tsui, H. L. Stormer, L. N. Pfeiffer, K. W. Baldwin, K. W. West, Strongly anisotropic transport in higher two-dimensional Landau levels. *Solid State Commun.* **109**, 389–394 (1999). doi:10.1016/S0038-1098(98)00578-X

4. R. A. Borzi, S. A. Grigera, J. Farrell, R. S. Perry, S. J. S. Lister, S. L. Lee, D. A. Tennant, Y. Maeno, A. P. Mackenzie, Formation of a nematic fluid at high fields in Sr3Ru2O7. *Science* **315**, 214–217 (2007). doi:10.1126/science.1134796 Medline

5. C. M. Varma, L. Zhu, Helicity order: Hidden order parameter in URu2Si2. *Phys. Rev. Lett.* **96**, 036405 (2006). doi:10.1103/PhysRevLett.96.036405 Medline

6. Y. Ando, K. Segawa, S. Komiya, A. N. Lavrov, Electrical resistivity anisotropy from self-organized one dimensionality in high-temperature superconductors. *Phys. Rev. Lett.* **88**, 137005 (2002). doi:10.1103/PhysRevLett.88.137005 Medline

7. V. Hinkov, D. Haug, B. Fauqué, P. Bourges, Y. Sidis, A. Ivanov, C. Bernhard, C. T. Lin, B. Keimer, Electronic liquid crystal state in the high-temperature superconductor $YBa_2Cu_3O_{6.45}$. *Science* **319**, 597–600 (2008). doi:10.1126/science.1152309 Medline

8. T.-M. Chuang, M. P. Allan, J. Lee, Y. Xie, N. Ni, S. L. Bud'ko, G. S. Boebinger, P. C. Canfield, J. C. Davis, Nematic electronic structure in the "parent" state of the iron-based superconductor $Ca(Fe_{1-x}Co_x)_2As_2$. *Science* **327**, 181–184 (2010). doi:10.1126/science.1181083 Medline

9. J.-H. Chu, J. G. Analytis, K. De Greve, P. L. McMahon, Z. Islam, Y. Yamamoto, I. R. Fisher, In-plane resistivity anisotropy in an underdoped iron arsenide superconductor. *Science* **329**, 824–826 (2010). doi:10.1126/science.1190482 Medline

10. S. Kasahara, H. J. Shi, K. Hashimoto, S. Tonegawa, Y. Mizukami, T. Shibauchi, K. Sugimoto, T. Fukuda, T. Terashima, A. H. Nevidomskyy, Y. Matsuda, Electronic nematicity above the structural and superconducting transition in $BaFe_2(As_{1-x}P_x)_2$. *Nature* **486**, 382–385 (2012). doi:10.1038/nature11178 Medline

11. R. M. Fernandes, A. V. Chubukov, J. Schmalian, What drives nematic order in iron-based superconductors? *Nat. Phys.* **10**, 97–104 (2014). doi:10.1038/nphys2877

12. S. A. Kivelson, E. Fradkin, V. J. Emery, Electronic liquid-crystal phases of a doped Mott insulator. *Nature* **393**, 550–553 (1998). doi:10.1038/31177

13. C. Wu, K. Sun, E. Fradkin, S.-C. Zhang, Fermi liquid instabilities in the spin channel. *Phys. Rev. B* **75**, 115103 (2007). doi:10.1103/PhysRevB.75.115103

14. L. Fu, Parity-breaking phases of spin-orbit-coupled metals with gyrotropic, ferroelectric, and multipolar orders. *Phys. Rev. Lett.* **115**, 026401 (2015). doi:10.1103/PhysRevLett.115.026401 Medline

15. T. C. Lubensky, L. Radzihovsky, Theory of bent-core liquid-crystal phases and phase transitions. *Phys. Rev. E Stat. Nonlin. Soft Matter Phys.* **66**, 031704 (2002). doi:10.1103/PhysRevE.66.031704 Medline

16. V. Kozii, L. Fu, Odd-parity superconductivity in the vicinity of inversion symmetry breaking in spin-orbit-coupled systems. *Phys. Rev. Lett.* **115**, 207002 (2015). doi:10.1103/PhysRevLett.115.207002 Medline

17. Y. Wang, G. Y. Cho, T. L. Hughes, E. Fradkin, Topological superconducting phases from inversion symmetry breaking order in spin-orbit-coupled systems. *Phys. Rev. B* **93**, 134512 (2016). doi:10.1103/PhysRevB.93.134512

18. M. R. Norman, Dichroism as a probe for parity-breaking phases of spin-orbit coupled metals. *Phys. Rev. B* **92**, 075113 (2015). doi:10.1103/PhysRevB.92.075113

19. C. A. Kendziora, I. A. Sergienko, R. Jin, J. He, V. Keppens, B. C. Sales, D. Mandrus, Goldstone-mode phonon dynamics in the pyrochlore $Cd_2Re_2O_7$. *Phys. Rev. Lett.* **95**, 125503 (2005). doi:10.1103/PhysRevLett.95.125503 Medline

20. J. P. Castellan, B. D. Gaulin, J. van Duijn, M. J. Lewis, M. D. Lumsden, R. Jin, J. He, S. E. Nagler, D. Mandrus, Structural ordering and symmetry breaking in $Cd_2Re_2O_7$. *Phys. Rev. B* **66**, 134528 (2002). doi:10.1103/PhysRevB.66.134528

21. J.-I. Yamaura, Z. Hiroi, Low Temperature Symmetry of Pyrochlore Oxide $Cd_2Re_2O_7$. *J. Phys. Soc. Jpn.* **71**, 2598–2600 (2002). doi:10.1143/JPSJ.71.2598

22. M. T. Weller, R. W. Hughes, J. Rooke, C. S. Knee, J. Reading, The pyrochlore family —A potential panacea for the frustrated perovskite chemist. *Dalton Trans.* **2004**, 3032–3041 (2004). doi:10.1039/b401787k Medline

23. J. C. Petersen, M. D. Caswell, J. S. Dodge, I. A. Sergienko, J. He, R. Jin, D. Mandrus, Nonlinear optical signatures of the tensor order in $Cd_2Re_2O_7$. *Nat. Phys.* **2**, 605–608 (2006). doi:10.1038/nphys392

24. I. A. Sergienko, S. H. Curnoe, Structural order parameter in the pyrochlore superconductor $Cd_2Re_2O_7$. *J. Phys. Soc. Jpn.* **72**, 1607–1610 (2003). doi:10.1143/JPSJ.72.1607

25. I. A. Sergienko, V. Keppens, M. McGuire, R. Jin, J. He, S. H. Curnoe, B. C. Sales, P. Blaha, D. J. Singh, K. Schwarz, D. Mandrus, Metallic "ferroelectricity" in the pyrochlore $Cd_2Re_2O_7$. *Phys. Rev. Lett.* **92**, 065501 (2004). doi:10.1103/PhysRevLett.92.065501 Medline

26. R. Jin, J. He, J. R. Thompson, M. F. Chisholm, B. C. Sales, D. Mandrus, Fluctuation effects on the physical properties of $Cd_2Re_2O_7$ near 200 K. *J. Phys. Condens. Matter* **14**, L117–L123 (2002). doi:10.1088/0953-8984/14/5/102

27. N. L. Wang, J. J. McGuire, T. Timusk, R. Jin, J. He, D. Mandrus, Optical evidence for mass enhancement of quasiparticles in pyrochlore $Cd_2Re_2O_7$. *Phys. Rev. B* **66**, 014534 (2002). doi:10.1103/PhysRevB.66.014534

28. H. Sakai, H. Kato, S. Kambe, R. E. Walstedt, H. Ohno, M. Kato, K. Yoshimura, H. Matsuhata, Low-temperature structural change and magnetic anomaly in superconducting Cd 2 Re 2 O 7. *Phys. Rev. B* **66**, 100509 (2002). doi:10.1103/PhysRevB.66.100509

29. Z. Hiroi, M. Hanawa, Y. Muraoka, H. Harima, Correlations and semimetallic behaviors in pyrochlore oxide $Cd_2Re_2O_7$. *J. Phys. Soc. Jpn.* **72**, 21–24 (2003). doi:10.1143/JPSJ.72.21

30. R. W. Boyd, *Nonlinear Optics* (Academic Press, 2008).

31. L. Wu *et al*., *Nat. Phys.* **13**, 350–355 (2017).

32. L. Zhao, D. H. Torchinsky, H. Chu, V. Ivanov, R. Lifshitz, R. Flint, T. Qi, G. Cao, D. Hsieh, Evidence of an odd-parity hidden order in a spin–orbit coupled correlated iridate. *Nat. Phys.* **12**, 32–36 (2016). doi:10.1038/nphys3517

33. L. Zhao *et al*., *Nat. Phys.* **13**, 250–254 (2017)

34. J. W. Harter, L. Niu, A. J. Woss, D. Hsieh, High-speed measurement of rotational anisotropy nonlinear optical harmonic generation using position-sensitive detection. *Opt. Lett.* **40**, 4671–4674 (2015). doi:10.1364/OL.40.004671 Medline

35. J. W. Harter, H. Chu, S. Jiang, N. Ni, D. Hsieh, Nonlinear and time-resolved optical study of the 112-type iron-based superconductor parent $Ca_{1-x}La_xFeAs_2$ across its structural phase transition. *Phys. Rev. B* **93**, 104506 (2016). doi:10.1103/PhysRevB.93.104506

36. Materials and methods are available as supplementary materials.

37. O. Vyaselev, K. Arai, K. Kobayashi, J. Yamazaki, K. Kodama, M. Takigawa, M. Hanawa, Z. Hiroi, Superconductivity and magnetic fluctuations in $Cd_2Re_2O_7$ via Cd nuclear magnetic resonance and Re nuclear quadrupole resonance. *Phys. Rev. Lett.* **89**, 017001 (2002). doi:10.1103/PhysRevLett.89.017001 Medline

38. H. Sakai, K. Yoshimura, H. Ohno, H. Kato, S. Kambe, R. E. Walstedt, T. D. Matsuda, Y. Haga, Y. Onuki, Superconductivity in a pyrochlore oxide, $Cd_2Re_2O_7$. *J. Phys. Condens. Matter* **13**, L785–L790 (2001). doi:10.1088/0953-8984/13/33/105

39. R. Jin, J. He, S. McCall, C. S. Alexander, F. Drymiotis, D. Mandrus, Superconductivity in the correlated pyrochlore $Cd_2Re_2O_7$. *Phys. Rev. B* **64**, 180503 (2001). doi:10.1103/PhysRevB.64.180503

40. M. Hanawa, Y. Muraoka, T. Tayama, T. Sakakibara, J. Yamaura, Z. Hiroi, Superconductivity at 1 K in $Cd_2Re_2O_7$. *Phys. Rev. Lett.* **87**, 187001 (2001). doi:10.1103/PhysRevLett.87.187001

41. J. He, R. Jin, B. C. Chakoumakos, J. S. Gardner, D. Mandrus, T. M. Tritt, Crystal growth, structure, and stoichiometry of the superconducting pyrochlore $Cd_2Re_2O_7$. *J. Electron. Mater.* **36**, 740–745 (2007). doi:10.1007/s11664-007-0087-7

42. J. Shamblin, M. Feygenson, J. Neuefeind, C. L. Tracy, F. Zhang, S. Finkeldei, D. Bosbach, H. Zhou, R. C. Ewing, M. Lang, Probing disorder in isometric pyrochlore and related complex oxides. *Nat. Mater.* **15**, 507–511 (2016). doi:10.1038/nmat4581 Medline

43. G. C. Lau, R. S. Freitas, B. G. Ueland, B. D. Muegge, E. L. Duncan, P. Schiffer, R. J. Cava, Zero-point entropy in stuffed spin-ice. *Nat. Phys.* **2**, 249–253 (2006). doi:10.1038/nphys270

44. S.-W. Huang, H.-T. Jeng, J.-Y. Lin, W. J. Chang, J. M. Chen, G. H. Lee, H. Berger, H. D. Yang, K. S. Liang, Electronic structure of pyrochlore $Cd_2Re_2O_7$. *J. Phys. Condens. Matter* **21**, 195602 (2009). doi:10.1088/0953-8984/21/19/195602 Medline

45. D. J. Singh, P. Blaha, K. Schwarz, J. O. Sofo, Electronic structure of the pyrochlore metals $Cd_2Os_2O_7$ and $Cd_2Re_2O_7$. *Phys. Rev. B* **65**, 155109 (2002). doi:10.1103/PhysRevB.65.155109

46. H. Harima, Electronic bandstructures on 5d-transition metal pyrochlore: $Cd_2Re_2O_7$ and $Cd_2Os_2O_7$. *J. Phys. Chem. Solids* **63**, 1035–1038 (2002). doi:10.1016/S0022-3697(02)00058-6

47. J. He, D. Hitchcock, I. Bredeson, N. Hickman, T. M. Tritt, S. N. Zhang, Probing lattice dynamics of $Cd_2Re_2O_7$ pyrochlore: Thermal transport and thermodynamics study. *Phys. Rev. B* **81**, 134302 (2010). doi:10.1103/PhysRevB.81.134302

48. D. M. Hatch, H. T. Stokes, *INVARIANTS* : Program for obtaining a list of invariant polynomials of the order-parameter components associated with irreducible representations of a space group. *J. Appl. Cryst.* **36**, 951–952 (2003). doi:10.1107/S0021889803005946

49. H. T. Stokes, D. M. Hatch, Coupled order parameters in the Landau theory of phase transitions in solids. *Phase Transit.* **34**, 53–67 (1991). doi:10.1080/01411599108205192

50. K. Aizu, General consideration of ferroelectrics and ferroelastics such that the electric susceptibility or elastic compliance is temperature independent in the prototypic phase. *J. Phys. Soc. Jpn.* **33**, 629–634 (1972). doi:10.1143/JPSJ.33.629

51. J.-C. Tolédano, P. Tolédano, *The Landau Theory of Phase Transitions* (World Scientific, 1987).

52. E. Bousquet, M. Dawber, N. Stucki, C. Lichtensteiger, P. Hermet, S. Gariglio, J.-M. Triscone, P. Ghosez, Improper ferroelectricity in perovskite oxide artificial superlattices. *Nature* **452**, 732–736 (2008). doi:10.1038/nature06817 Medline

53. Y. S. Oh, X. Luo, F.-T. Huang, Y. Wang, S.-W. Cheong, Experimental demonstration of hybrid improper ferroelectricity and the presence of abundant charged walls in $(Ca,Sr)_3Ti_2O_7$ crystals. *Nat. Mater.* **14**, 407–413 (2015). doi:10.1038/nmat4168 Medline

54. H. T. Stokes, D. M. Hatch, H. M. Nelson, Landau, Lifshitz, and weak Lifshitz conditions in the Landau theory of phase transitions in solids. *Phys. Rev. B Condens. Matter* **47**, 9080–9083 (1993). doi:10.1103/PhysRevB.47.9080 Medline

55. A. B. P. Lever, *Inorganic Electronic Spectroscopy* (Elsevier, 1984).